Chemical Science

ROYAL SOCIETY OF CHEMISTRY

EDGE ARTICLE

View Article Online
View Journal | View Issue

Cite this: *Chem. Sci.*, 2024, **15**, 17032

All publication charges for this article have been paid for by the Royal Society of Chemistry

Received 25th May 2024
Accepted 6th September 2024

DOI: 10.1039/d4sc03424d

rsc.li/chemical-science

Tumor oxygen microenvironment-tailored electron transfer-type photosensitizers for precise cancer therapy†

Yiting Yang, [a] Yafu Wang, [a] Yang Liu,[a] Kui Wang, [a] Ge Wang, [b] Yonggang Yang,[a] Won Jun Jang, [d] Tony D. James, [ac] Juyoung Yoon *[d] and Hua Zhang *[a]

The oxygen level in a tumor typically exhibits complex characteristics, ranging from mild hypoxia to moderate and even severe hypoxia. This poses significant challenges for the efficacy of photodynamic therapy, where oxygen is an essential element. Herein, we propose a novel therapeutic strategy and develop a series of lipid droplet-targeting photosensitive dyes (**Ser-TPAs**), *i.e., in situ* synergistic activation of two different electron transfer-type reactions. Based on this strategy, **Ser-TPAs** can synergistically generate $O_2^{\bullet-}$ and nitrogen radicals regardless of the oxygen content, which results in a sustained high concentration of strongly oxidizing substances in the lipid droplets of cancer cells. As such, **Ser-TPAs** exhibited inhibitory activity against tumor growth *in vivo*, resulting in a significant reduction in tumor volume ($V_{\text{experimental group}} : V_{\text{control group}} \approx 0.07$). This strategy offers a conceptual framework for the design of innovative photosensitive dyes that are suitable for cancer therapy in complex oxygen environments.

Introduction

Photodynamic therapy (PDT) has been recognized as a novel minimally invasive targeted approach for tumor treatment in clinical practice over recent years.[1–3] PDT employs photosensitive dyes to initiate a series of photochemical reactions upon specific light irradiation,[4,5] leading to the instantaneous formation of free radicals ($O_2^{\bullet-}$, $^{\bullet}OH$, *etc.*) or singlet oxygen ($^1O_2$) *via* electron transfer or energy transfer due to the different oxygen environments of the solid tumor lesion, respectively.[6–8] Ultimately, this process induces the irreversible apoptosis of solid tumors. It is apparent that oxygen, light and photosensitive dyes are necessary elements for the PDT treatment of solid tumors. However, hypoxia is a common characteristic observed in solid tumors.[9,10] Tumor lesions often exhibit mild (>2.5% O_2) to moderate (1–2% O_2) or even severe (<0.01% O_2) hypoxia due to imbalances in solid tumor growth and the poorly organized vasculature.[11] Moreover, the oxygen content in solid tumors is highly variable and can change significantly due to reduced internal oxygen supply with increasing tumor volume. Such hypoxia environments not only exacerbate the complexity of the tumor microenvironment but also seriously limit the therapeutic effect of PDT treatment strategies. Functioning as the core element of PDT, photosensitive dyes offer an effective approach toward addressing the challenges mentioned above, and developing photosensitive dyes that are capable of self-regulating different electron transfer-type reactions based on different levels of oxygen at tumor sites holds great promise for treating solid tumors with varying degrees of hypoxia.

In recent years, a range of targeting photosensitive dyes exhibiting excellent biocompatibility and metabolic capacity have been reported, some of which have been used for clinical photodynamic therapies,[12–17] such as Photofrin, verteporfin, Foscan, *etc.* These dyes can generate singlet or free radical oxygen at tumor tissues upon irradiation with visible light (*ca.* 650 nm). However, despite their approval for cancer intervention, these photosensitive dyes still face significant limitations due to their dependence on oxygen. Consequently, researchers in this field are focusing on addressing the issue of oxygen dependency.[18–31] A photosensitive dye (protoporphyrin IX, PPIX) coordinated with Cu(II) has been reported to enhance intersystem conversion from the singlet excited state to a triplet excited state *via* the stretching vibrations of N–H bonds.[18] This enhancement effect successfully improves the production of

[a]*Key Laboratory of Green Chemical Media and Reactions, Ministry of Education, Collaborative Innovation Centre of Henan Province for Green Manufacturing of Fine Chemicals, Key Laboratory of Organic Functional Molecules and Drug Innovation, Henan Province, School of Chemistry and Chemical Engineering, Henan Normal University, Xinxiang, Henan 453007, P. R. China. E-mail: zhh1106@htu.edu.cn*

[b]*College of Basic Medicine, Xinxiang Medical University, Xinxiang, Henan 453007, P. R. China*

[c]*Department of Chemistry, University of Bath, Bath, BA2 7AY, UK*

[d]*Department of Chemistry and Nanoscience, Ewha Womans University, Seoul 03760, Korea. E-mail: jyoon@ewha.ac.kr*

† Electronic supplementary information (ESI) available. See DOI: https://doi.org/10.1039/d4sc03424d

$^1O_2$ under mild hypoxia (>2.5% O_2). Meanwhile, a mitochondria-targeting photosensitive dye (^{mito}aPS) with dual activation can generate $^1O_2$ through combined classical PDT reactions (*i.e.* type-I and type-II), even under low oxygen conditions as low as 1% O_2.[19] However, these photosensitive dyes have limited efficacy in severe hypoxic tumors with oxygen content equal to or less than 0.01%. To overcome the oxygen dependence limitation of PDT, Peng and Kim developed a unimolecular photodynamic O_2 economizer (PDOE) containing a mitochondria-targeted $O_2^{\bullet-}$ generator (SORgenTAM). Therefore, using SORgenTAM, ensures the hypoxic environment can be overcome, enabling type-I PDT with significantly reduced dependence on oxygen levels (2%).[20] Significantly, Peng and Fan reported the development of photosensitive dyes (NBEX) based on a new mechanism known as the type-III PDT reaction that does not require oxygen at all.[21] When NBEX is excited by light, the excitation energy or electrons can be directly transferred to RNA to effectively destroy RNA and eliminate tumor cells even under hypoxic or anaerobic conditions. This research provides both conceptual insights and practical approaches for overcoming the limitations of phototherapeutics, while offering new design perspectives for photosensitive dyes under conditions of extremely low oxygen content (<0.01%). This previous research, which confirms that it is possible to ablate tumors using PDT even at low oxygen levels, provided us with the inspiration and motivation for the research described below.

Herein, we propose a novel strategy for a photosensitive dye (Fig. 1), that is, *in situ* synergistic activation of different electron transfer-type reactions based on the tumor oxygen microenvironments in the lesion area. Using this concept, a series of triphenylamine-based photosensitive dyes were designed and synthesized, including ((*E*)-4-(4-nitrostyryl)-*N*,*N*-diphenylaniline, **NO_2-TPA**, (*E*)-4-(4-aminostyryl)-*N*,*N*-diphenylaniline, **NH_2-TPA**, and (*E*)-*N*,*N*-diphenyl-4-styrylaniline, **H-TPA**), as depicted in Fig. 1. These photosensitive dyes should generate superoxide radical ions ($O_2^{\bullet-}$) until the oxygen concentration at the lesion sites decreases to < 0.01%, *i.e.* O_2-type process. Subsequently, under severe hypoxic conditions (<0.01% O_2), the excited singlet state of the photosensitive dye induces nitrogen radical formation through electron transfer facilitated by the tumor marker coenzyme upon light irradiation at the lesion sites (NAD^+-type process). Consequently, these photosensitive dyes should exhibit remarkable efficacy against both hypoxic tumors and severely hypoxic tumors and display excellent performance in solid tumors with complex oxygen environments.

Results

Molecular design and synthesis

To enhance photodynamic efficacy, this research provides an *in situ* synergistic activation strategy, *i.e.* the synergistic activation of two different electron transfer-type reactions according to different oxygen levels. One is an O_2-type process and the other is a NAD^+-type process (Fig. 1). Nitroreductase (NTR), a marker enzyme for hypoxic solid tumors, was selected as the initiator of the synergistic electron transfer-type reactions to enhance targeting of the photosensitive dye. Since NTR is overexpressed in hypoxic tumors and its expression is enhanced with an increase of the hypoxic degree,[32,33] nitrobenzene, serving as the specific recognition group for NTR, was incorporated into the one end of the molecular skeleton (styryl) in the molecular design (see Fig. 1), while nicotinamide-adenine dinucleotide (NAD^+), acting as a coenzyme facilitating electron transport of the photosensitive dye in living organisms,[34] was chosen along with NTR to construct a complete system regulating photosensitive activity using two different electron transfer-type reactions. Importantly, the introduction of the nitrobenzene effectively inhibits the electron transfer from the photosensitive dye to biological substrates in non-tumor lesions under the influence of NAD^+,

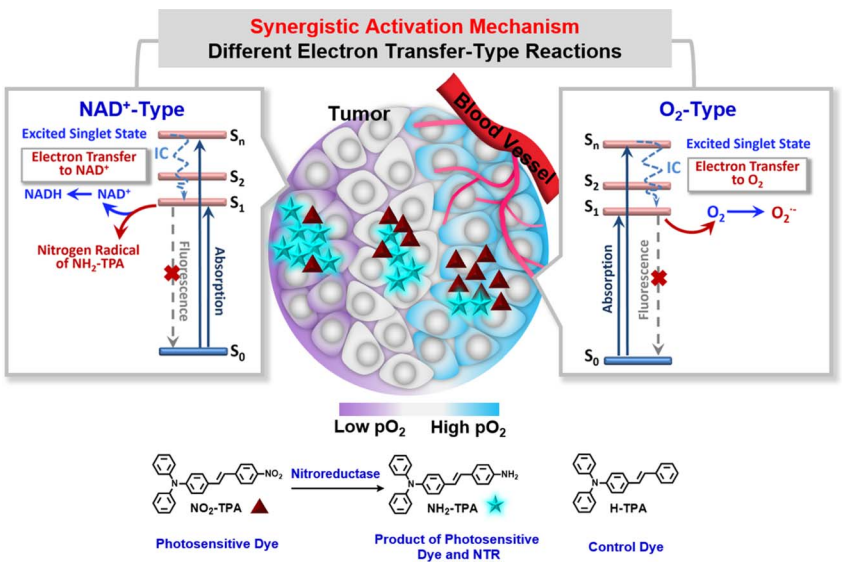

Fig. 1 Chemical structures of compounds (NO_2-TPA, NH_2-TPA and H-TPA) and schematic diagram of the *in situ* synergistic activation mechanism for PDT activation.

which can significantly improve the targeting efficiency of photodynamic therapy. Furthermore, linking *N*,*N*-diphenylaniline to the other side of the styryl enhances the intramolecular charge-transfer (ICT) effect and provides potential for nitrogen radical formation under enzymatic regulation. A series of photosensitive dyes (**Ser-TPAs**, *i.e.* (*E*)-4-(4-nitrostyryl)-*N*,*N*-diphenylaniline, **NO_2-TPA**, (*E*)-4-(4-aminostyryl)-*N*,*N*-diphenylaniline, **NH_2-TPA**, and (*E*)-*N*,*N*-diphenyl-4-styrylaniline, **H-TPA**), were prepared and their molecular structures were confirmed by ^{1}H NMR, ^{13}C NMR, and Q-TOF-MS analytical data available in the ESI.†

Spectral behavior and mechanistic analysis in solution during the O_2-type process

The spectral behavior was examined and analyzed using UV-vis absorption, two-photon absorption, fluorescence, phosphorescence, electron paramagnetic resonance (EPR) spectra and so on. Table S1† shows that the molar extinction coefficient (ε) of **NO_2-TPA** is 2.66 × 10^4 M^{-1} cm^{-1} in H_2O (λ_{ex} = 456 nm). The two-photon absorption cross section of **NO_2-TPA** was measured from 750 nm to 840 nm and exhibited a significant capacity for two-photon absorption within this range. A maximum absorption cross section of 394 GM was observed at 750 nm (1 GM = 10^{-50} cm^4 s per photon, Fig. S1†), indicating its suitability for excitation by near-infrared light.[35] And stability experiments indicate that **NO_2-TPA** is suitable for use in physiological environments (Fig. S2†). These findings confirmed the fundamental molecular properties of the system for potential applications in PDT under long wavelength excitation.

In the free state, **NO_2-TPA** (10 μM) exhibited a weak fluorescence quantum yield (Φ_{flu} = 0.27%, Table S1 and Fig. S3†) with an emission peak at 660 nm in H_2O. Additionally, there was also negligible phosphorescence observed at 640 nm with extremely low intensity (Fig. S4†), which can be attributed to the quenching effect of $-NO_2$. We calculated the electron hole separation of **NO_2-TPA** and **NH_2-TPA**, as shown in Fig. 2A and the electron and hole distance of **NO_2-TPA** was 9.53 Å, which was much larger than the 1.51 Å of **NH_2-TPA**. The greater the distance, the greater the energy loss for the **NO_2-TPA** electron transition, and consequently the quenching of the fluorescence.[36] The absence of intersystem crossing (ISC) from the excited singlet state (S_1) to the excited triplet state (T_1) was confirmed by theoretical calculations ($\Delta E_{S_1-T_1}$ = 0.95 eV, K_{isc} (S_1–T_1) = 1.6 × 10^4 s^{-1} and K_{risc} (S_1–T_1) = 0.40 × 10^4 s^{-1}, Table S2†). When 2′,7′-dichlorodihydrofluorescein (DCFH), a tracer agent for ROS, was used, no spectral changes were observed under light irradiation regardless of the presence or absence of oxygen (Fig. S5b†). Moreover, in the presence of NAD^+, no signal enhancement of DCFH was observed in the **NO_2-TPA** test system (Fig. S6†). EPR spectra also confirmed the absence of any signals corresponding to $O_2^{\bullet-}$, $^{\bullet}OH$, $^1O_2$ and other reactive oxygen species (Fig. 2B, blue line and red line, Fig. S7†). These results indicate that **NO_2-TPA** did not produce ROS including $O_2^{\bullet-}$, $^{\bullet}OH$, and $^1O_2$, suggesting that traditional type-I or type-II PDT reactions do not occur, nor any new types of PDT reaction are initiated by **NO_2-TPA** in the free state. This characteristic is expected to significantly enhance PDT targeting efficiency towards cancer cells.

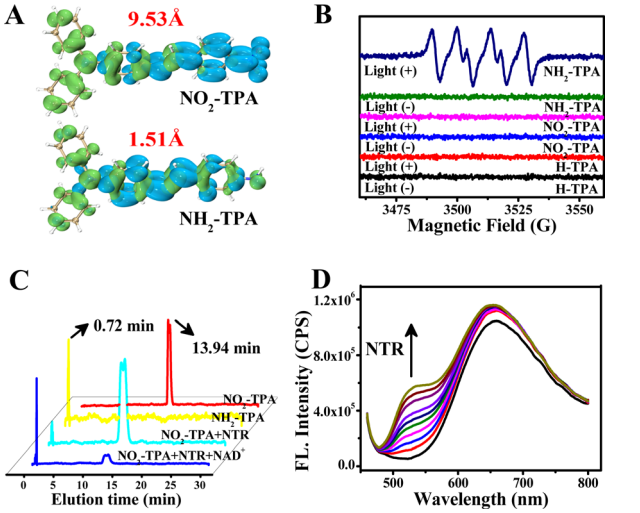

Fig. 2 (A) Electron–hole distributions of NO_2-TPA and NH_2-TPA. The green regions represent electrons, and the blue regions represent holes. NO_2-TPA has a larger distance dispersion of electrons and holes (9.53 Å) than NH_2-TPA (1.51 Å), resulting in increased energy loss and lower fluorescence. (B) EPR spectra of NO_2-TPA, NH_2-TPA and H-TPA with or without light irradiation. The trapping agent was DMPO, and the test solution was methanol. Light (+): with light irradiation; light (−): without light irradiation. (C) NO_2-TPA, NH_2-TPA and the products of NO_2-TPA reacting with NTR and NAD^+ evaluated by HPLC. (D) Fluorescence response of NO_2-TPA (10 μM) to NTR (0–4.67 μg mL^{-1}) in H_2O at 37 °C.

Upon encountering the tumor marker enzyme NTR,[37,38] **NO_2-TPA** exhibits distinct and stable changes in its fluorescence spectra within 150 s (Fig. S8†). HPLC revealed that **NO_2-TPA** (red line in Fig. 2C, 13.94 min) undergoes conversion to **NH_2-TPA** (yellow line and blue line in Fig. 2C, 0.72 min) under the action of NTR, which can be triggered by a minimal overexpressed concentration of NTR (Fig. S9†). Furthermore, due to the changes in the molecular structure, the fluorescence intensity at 660 nm remains stable while the intensity at 525 nm gradually increases with increasing concentration of NTR (Fig. 2D). However, Φ_{flu} is still very low at 0.31% (see Table S1†). The phosphorescence is also observed to be extremely weak (Fig. S4†). We used EPR spectroscopy to further investigate the type of ROS generation during the O_2-type process in the presence of oxygen. The EPR spectra exhibited a strong specific signal for $O_2^{\bullet-}$ (Fig. 2B, navy blue line), but no signal for $^1O_2$ (Fig. S7B†). The fluorescence spectra with different tracer agents for different kinds of ROS were used to detect this process (Fig. S5†). The above results confirmed that $O_2^{\bullet-}$ is indeed generated by **NH_2-TPA**, the product of **NO_2-TPA** in an O_2-type process, which occurs when the oxygen content is >0.01%.

To elucidate the mechanism of the O_2-type process, transient absorption spectroscopy was used to determine the T_1 state of **NO_2-TPA**, **NH_2-TPA** and the contrastive molecule **H-TPA** (Fig. S11†). The spectra reveal the absence of the T_1 state for both **NO_2-TPA** and **H-TPA**, while the T_1 signal in **NH_2-TPA** was found to be negligible. Thus, there is no ISC from S_1 to T_1 in **NO_2-TPA**,

NH_2-TPA and **H-TPA**, which can be further supported by the theoretical calculations (see Table S2†). To further confirm the mechanism of $O_2^{\bullet-}$ generation, we determined the electron transfer capacity of **NO_2-TPA** and **NH_2-TPA** in their respective S_1 states as well as their oxidation potentials. Upon addition of 7,7,8,8-tetracyanoquinodimethane (TCNQ) at a concentration of 40 μM as an electron acceptor into each solution, respectively, a significant decrease in the fluorescence spectra of **NH_2-TPA** was observed, but no such phenomenon was observed for the fluorescence spectra of **NO_2-TPA** (Fig. S12†). In other words, only **NH_2-TPA** can transfer electrons to O_2 from the S_1 state (O_2-type process). The above processes are all completed with normal oxygen levels. However, the oxygen levels inside the tumors are complicated and it is necessary to investigate how the electron transfer reaction works at various oxygen levels.

Spectral behavior and mechanistic analysis in solution during the NAD^+-type process

The intricate oxygen environment is a prominent feature in malignant tumors. The levels of NTR and NAD^+ exhibit a significant increase when the content of O_2 drops to as low as 0.01% (severe hypoxia, NAD^+-type process). Notably, the electron transfer ability of NAD^+ is greatly enhanced *in situ*.[39–41] From Fig. 3A, a gradual decrease in fluorescence intensity at 656 nm is accompanied by an incremental enhancement in intensity at 540 nm with increasing concentrations of NTR and NAD^+. However, despite this observation, the fluorescence intensity remains relatively low with a Φ value of only 0.52%, and no phosphorescence was detected (Table S1†). The presence of electron holes was detected by EPR spectroscopy (Fig. S7C and D†), which verified the ability of the NAD^+-type process to generate nitrogen radical signals under hypoxic conditions. Subsequently, triphenylamine nitrogen centered radicals produced by the photochemical reaction of **NH_2-TPA** and NAD^+ were detected. The results are presented in Fig. 3B, and the EPR spectra displayed a three-line splitting pattern consistent with that of the triphenylamine nitrogen radical.[42] All the above results confirmed that a novel reaction generating a nitrogen radical occurred under electron transfer mediated by NAD^+ at extremely low oxygen levels (<0.01%).

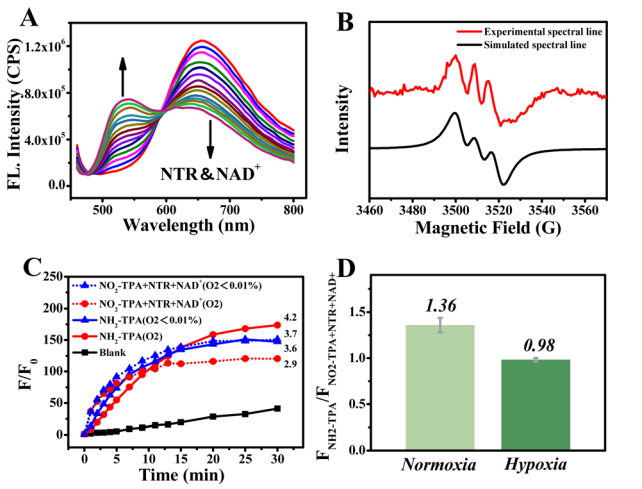

Fig. 3 (A) Fluorescence response of **NO_2-TPA** (10 μM) to both NTR (0–4.67 μg mL^{-1}) and NAD^+ (66.7 μM) in H_2O. All tests were carried out at 37 °C. (B) EPR spectra of the nitrogen centered radical for the photochemical reaction between **NH_2-TPA** and NAD^+ (experimental: red line; simulated: black line). (C) Relative changes in the fluorescence intensity of DHR123 (40 μM) an indicator for $O_2^{\bullet-}$ measured when **NH_2-TPA** (10 μM), **NO_2-TPA** (10 μM), NTR and NAD^+ were subjected to light irradiation. Note: because the wavelength of the $O_2^{\bullet-}$-specific recognition probe DHE and the photosensitive dye involved in this paper interfere with each other, DHR123 was selected as an alternative probe to carry out the test. (D) Bar plots for the ratio of ROS generated by **NH_2-TPA** relative to **NO_2-TPA** reacting with NTR and NAD^+ under normoxic and hypoxic conditions.

To characterize nitrogen radical production for the different oxygen levels, the fluorescence spectra were used during the NAD^+-type process with dihydrorhodamine 123 (DHR123) as an indicator for free radicals.[43] Due to varying NTR activity under different oxygen conditions, the amount of **NH2-TPA** produced is different, so there will be a different PDT effect. As such, Fig. 3C and D display signal enhancements with different oxygen levels and even at oxygen levels <0.01%. Fig. S5† also shows the same results using DCFH as an indicator for ROS including nitrogen radicals. These above results indicated that the NAD^+-type process was initiated during the process of oxygen deprivation and could generate nitrogen-radical species for continuous photodynamic therapy.

To investigate the reaction mechanism in the second process (O_2 <0.01%), the electron binding capacities of **NO_2-TPA**, **H-TPA** and **NH_2-TPA** were calculated by molecular docking and theoretical calculations (Fig. 4). The results are depicted in Fig. 4A and indicate significant changes in the predominant conformations of these molecules. After binding with NAD^+, **NH_2-TPA** exposes the single electron pair from N more extensively than before. The electron cloud density on the nitrogen atom of triphenylamine of **NO_2-TPA**, **H-TPA** and **NH_2-TPA** in the S_1 state is −0.061, −0.093 and −0.083, respectively (Fig. 4B), indicating an increasing trend in the electron donating abilities: **NO_2-TPA** < **H-TPA** < **NH_2-TPA**. This observation is further supported by the REDOX potential of the S1 state (Table S3†). Consequently, **NH_2-TPA** exhibits a higher propensity to form the nitrogen radical by donating electrons from its N atom compared to other compounds such as **NO_2-TPA**, which does not exhibit this behavior in the S_1 state. Therefore, the NAD^+-type process mainly involves an electron transfer-type reaction between **NH_2-TPA** and NAD^+, leading to the generation of nitrogen radical signals specifically within severely hypoxic tumors (<1% O_2).

Synergistic mechanism of two electron transfer-type reactions (O_2-type and NAD^+-type processes)

It is well known that organisms have extraordinarily complex microenvironments, notably at the location of lesions, where the concentrations of O_2, NTR and NAD^+ are highly variable. Activating either the O_2-type process or NAD^+-type process in this environment. Therefore, it is important to use both the O_2-type and NAD^+-type processes in concert in a biological environment. REDOX potentials were used to confirm the

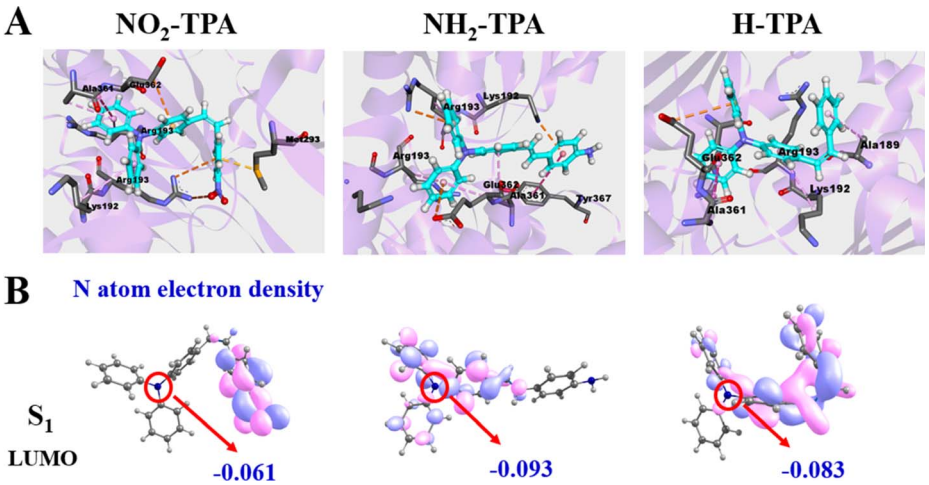

Fig. 4 (A) Molecular docking diagrams of NO_2-TPA, NH_2-TPA and H-TPA with NAD^+ respectively. (B) Molecular calculations and electron density on the nitrogen atom for optimal configurations of NO_2-TPA, NH_2-TPA, and H-TPA binding to NAD^+.

occurrence of these two processes in living organisms. The REDOX potentials of $O_2/O_2^{\bullet-}$ and NAD^+/NADH are −0.33 V and −0.32 V, respectively, *vs.* standard electrode potential (Fig. S13†).[44,45] Meanwhile, the excited singlet state of **NH_2-TPA** had a REDOX potential of −2.60 V (Fig. S13†). So, **NH_2-TPA** could react with O_2 to form $O_2^{\bullet-}$ *via* the O_2-type process and with NAD^+ to form nitrogen radicals *via* the NAD^+-type process. Significantly, the two processes can occur in concert in living organisms. Throughout the synergistic process, O_2 will be consumed until it is exhausted. Therefore, by using the synergistic effect of both the O_2-type process and the NAD^+-type process, the progression and metastasis of the tumor will be significantly reduced.

Application and analysis in living cells

Given the synergistic activation mechanism of such photosensitive dyes, the HepG-2 cell line was selected to explore possible applications and the mechanism in living cells. Firstly, the intracellular distribution was investigated. We calculated log *P* values for the molecules **NO_2-TPA** and **NH_2-TPA**, which are 6.8 and 5.9, respectively. **NO_2-TPA** is highly lipophilic based on quantitative structure–activity relationship analysis and was expected to accumulate in lipid droplets due to its membrane permeability.[46] At the same time, Fig. S14† reveals that **NO_2-TPA** was predominantly localized in a small organelle known as a lipid droplet (diameter as small as 40 nm), which plays crucial roles in lipid metabolism and storage, membrane transport, and protein degradation, and has become an important target for cancer therapy.[47,48] These characteristics enable **NO_2-TPA** to rapidly generate high concentrations of strong oxidizing substances (such as $O_2^{\bullet-}$, nitrogen radicals, *etc.*) in the intracellular region. Consequently, these two different electron transfer-type reaction processes can enhance efficacy toward cancer cells.[49]

Subsequently, different oxygen contents were modeled in HepG-2 cells to further validate the synergetic function of O_2-type and NAD^+-type reaction processes. DCFH-DA, DHR123 and Singlet Oxygen Sensor Green (SOSG, a fluorescent indicator for $^1O_2$) were added into three cell models with different oxygen contents (*i.e.*, 21%, 2.5% and <0.01%). Under a normal oxygen environment (21% oxygen content), an apparent fluorescence intensity was observed upon incubation of DHR123 (Fig. 5A) after 3 minutes of light irradiation in cancer cells expressing high levels of NTR. Moreover, the fluorescence intensity decreased as the oxygen content decreased (2.5% and <0.01%), and DCFH-DA exhibited a slight increase in fluorescence intensity for the different cell models with varying oxygen content (Fig. 5B). Simultaneously, no signal for $^1O_2$ was detected regardless of the amount of O_2 (Fig. 5C). These results obtained from both solution-based experiments and living cells collectively confirm that as the O_2 content decreases, there is a concomitant decrease in the generation of $O_2^{\bullet-}$, while an increase in the generated amount of nitrogen radical occurs. This highlights an intelligent synergistic activation mechanism involving a gradual throttling of the O_2-type reaction process (Fig. 1, O_2-type) along with the activation of the NAD^+-type reaction process (Fig. 1, NAD^+-type) upon decreasing oxygen levels. A methyl thiazolyl tetrazolium (MTT) colorimetric assay was used to verify the targeted killing ability toward cancer cells. The results indicated that **NO_2-TPA** (5 μM) exhibited significant cytotoxicity (21% O_2: 59% death rate, 2.5% O_2: 54% death rate and 0% O_2: 41% death rate) specifically toward HepG-2 cells under irradiation. Compared with similar photosensitive dyes reported previously, **NO_2-TPA** exhibited potent cell phototoxicity as well as good cancer cell targeting ability (Table S4†). Additionally, **NO_2-TPA** effectively inhibited cell proliferation in a concentration-dependent manner as evidenced by its IC_{50} value for HepG-2 cells being determined to be 4.3 μM (Fig. S15†).

To further elucidate the underlying cause of the elevated mortality rate, a mitochondrial membrane potential assay was performed with HepG-2 cells, since it represents an early event in the apoptosis cascade reaction.[50] The imaging results (Fig. S16†) revealed a gradual decrease in fluorescence intensity in the red channel (580–620 nm), accompanied by a corresponding increase in fluorescence intensity in the green channel (500–550

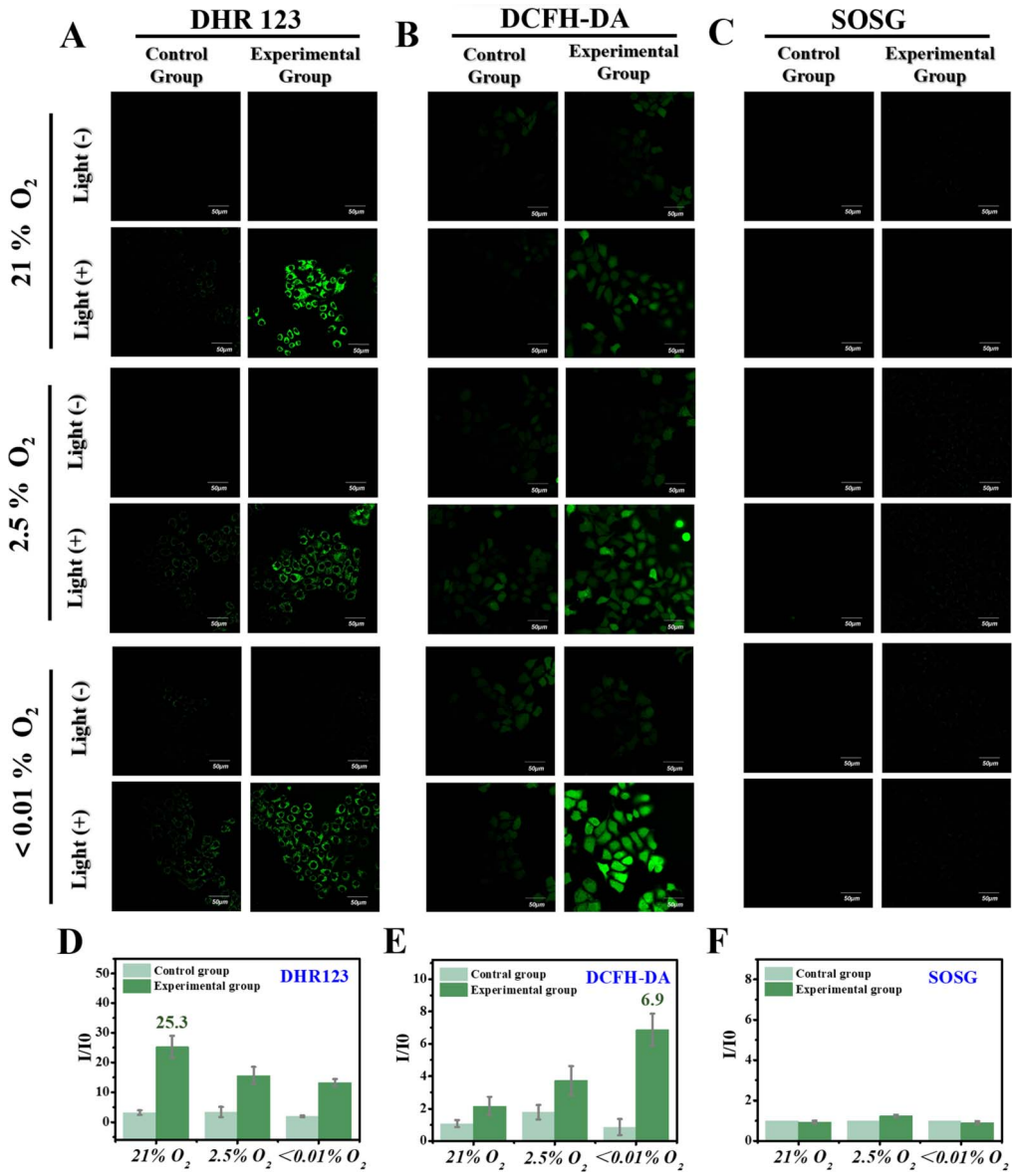

Fig. 5 The $O_2^{\bullet-}$ ((A) DHR 123, 6 μM, Ex: 488 nm, and green channel: 500–550 nm), ROS ((B) DCFH-DA, 6 μM, Ex: 488 nm, and green channel: 500–550 nm) and $^1O_2$ ((C) SOSG, 5 μM, Ex: 488 nm, and green channel: 500–550 nm) generation ability of **NO_2-TPA** (6 μM) in HepG-2 cells with different oxygen levels. The irradiation time was 3 min. Scale bars: 50 μm. (D–F) Fluorescence histogram of DHR123, DCFH-DA and SOSG at < 0.01%, 2.5% and 21% O_2 concentrations.

nm) during 0–20 min of irradiation. These findings indicate a reduction in mitochondrial membrane potential and subsequent initiation of programmed cell death. High-throughput flow cytometric analysis confirmed a significant increase in apoptotic cell population upon incubation with **NO_2-TPA** and **NH_2-TPA** under irradiation (Fig. S17†).

In vivo applications

The feasibility of **NO_2-TPA** for tumor treatment in mice was further investigated. Various levels of oxygen content in solid tumors (ranging from normal oxygen to mild, moderate, and severe hypoxia) were validated for their photodynamic therapeutic effect. Fig. S18† indicates that a wide range of fluorescence intensity changes were observed when the tumor tissue section was incubated with $[Ru(dpp)_3]Cl_2$ as an oxygen-indicating probe, confirming the highly intricate nature of O_2 content in solid tumors.[51] The *in vivo* performance of **NO_2-TPA** was evaluated using tumor-bearing mice and a Night OWL II LB 983 imaging system when the solid tumors reached approximately 120 mm^3. Fig. S19† illustrates the detection of distinct fluorescence at 530–570 nm following intratumoral injection of **NO_2-TPA**. Over time, the fluorescence intensity gradually increased and peaked at 30 minutes post-injection, suggesting that this time point would be optimal for subsequent PDT.

For the PDT experiments, we chose NU/NU tumor-bearing mice. Tumors were treated with **NO_2-TPA/NH_2-TPA** by

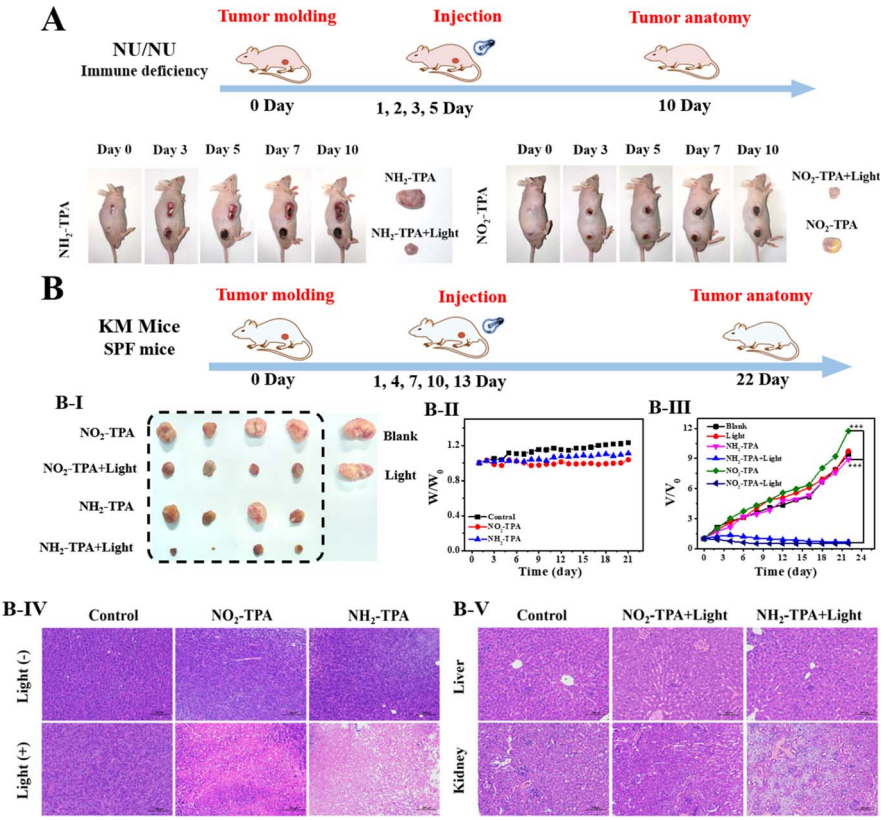

Fig. 6 (A) Photodynamic therapeutic efficiency of NO_2-TPA and NH_2-TPA in S180 tumor-bearing NU/NU mice. On days 1, 4 and 7, NO_2-TPA/NH_2-TPA (1 mM, 20 μL) and light were delivered, and photographs were collected during the 10 days of monitoring. (B) Photodynamic therapeutic efficiency of NO2-TPA and NH2-TPA toward S180 tumor-bearing KM mice. NO_2-TPA/NH_2-TPA (1 mM, 20 μL) and light were applied on days 1, 4, 7, 10 and 13. Tumor volumes were measured one day apart and mice were weighed daily. Tumors were stripped after 22 days to obtain the photographs. (B(I)) Images of tumors harvested in mice from different groups after 22 days of treatment. (B(II)) Tumor volume changes in KM mice subjected to various treatments. (B(III)) Body weight changes of KM mice subjected to various treatments. ***($P < 0.001$). (B(IV and V)) H&E staining analysis of tumor tissues, liver and kidneys following various therapies. The liver and kidney experimental groups were from mice treated by injection and illumination, and the control group was from mice without any treatment. Scale bars: 100 μm.

injection and light irradiation was performed on days 1, 2, 3, and 5, and the tumor was dissected after the tenth day of feeding. As shown in Fig. 6A, compared to the **NO_2-TPA/NH_2-TPA** group, the experimental group (**NO_2-TPA/NH_2-TPA** + light irradiation group) exhibited significant ablation. Encouraged by these results, in order to better verify the universality and effectiveness of the photosensitizer, we used normal strain KM mice to replace immunodeficient mice NU/NU, and extended the feeding time used for the subsequent experiments. The tumors were treated by injecting with **NO_2-TPA** and then subjecting them to light irradiation on days 1, 4, 7, 10 and 13. Fig. 6B(III) indicates that the tumor volume ratio (V/V_0) in the control group and blank group was 9.4 (control group), 11.7 (**NO_2-TPA** group) and 9.7 (light irradiation group). Remarkably, the experimental group (**NO_2-TPA** + light irradiation group, the treatment period = 22 days) exhibited a remarkable tumor regression effect with a $V_{\text{experimental group}}/V_{\text{control group}}$ of only 0.07. The tumor suppression effects of the control groups, blank groups and experimental groups were further analyzed using hematoxylin–eosin staining (H&E). Fig. 6B(IV) indicates significant cell apoptosis in the experimental groups (**NO_2-TPA** + light irradiation group), while extensive cell damage was not observed in the other groups. Furthermore, no abnormal changes in body weight were observed during treatment for any of the mice (Fig. 6B(II)). Additionally, there were no noticeable signs of cell necrosis or inflamed lesions in the liver and kidneys of the experimental group (Fig. 6B(V)), highlighting the biocompatibility and applicability of **NO_2-TPA** toward *in vivo* systems.

Conclusions

In summary, to overcome the limitations imposed on the efficacy of PDT by the complex oxygen environment in solid tumors, we have developed a series of novel styryl molecular skeleton-based photosensitive dyes (**Ser-TPAs**). The presence of specific recognition groups attached to ends of the molecular skeleton enables synergistic activation of two different electron transfer-type reactions at varying oxygen levels at tumor lesions. Under normoxic conditions, electron transfer between **Ser-TPAs** and oxygen molecules *via* an O_2-type process generates $O_2^{\bullet-}$, while electron transfer between **Ser-TPAs** and NAD^+ through a NAD^+-type process results in the formation of a nitrogen radical. Consequently, as oxygen is depleted and extreme

hypoxia prevails in the tumor lesion, there is a gradual decrease in the efficiency of the O_2-type process mediated by **Ser-TPAs**, whereas the enhancement of the NAD^+-type process takes place. Electron transfer occurs between **Ser-TPA** and NAD^+, a biological enzyme, resulting in the generation of a nitrogen radical with strong oxidation capabilities, which increases with higher levels of hypoxia. The synergistic interaction between the nitrogen radicals and $O_2^{\bullet-}$ allows for continuous production of high concentrations of potent oxidizing substances by **Ser-TPAs** in the tumor lesion, thereby maintaining an excellent photodynamic therapeutic effect and achieving effective tumor photoablation. Furthermore, **Ser-TPAs** exhibit remarkable tumor targeting ability as they are exclusively activated in cancer cells. These findings emphasize the potential of **Ser-TPAs** as a valuable tool for hypoxic tumor therapy while providing new perspectives for the design and development of novel photosensitive dyes to treat complex cancers using co-activation strategies involving both electron transfer-type reactions.

Data availability

The authors confirm that the data supporting the findings of this study are available within the article [and/or its ESI†].

Author contributions

Y. T. Y., J. Y. Y. and H. Z. proposed the concept and supervised the work; Y. T. Y. performed the synthesis of compounds and participated in all experimental processes. Y. F. W. and G. W. involved in mouse tumor model construction and *in vivo* testing. Y. L., K. W. and Y. G. Y. performed quantitative theoretical calculations. Y. T. Y., W. J., T. D. J., J. Y. Y. and H. Z. contributed to the discussion and provided suggestions. Y. T. Y. and H. Z. wrote the manuscript. All authors discussed the results and commented on the manuscript.

Conflicts of interest

The authors declare no competing interests.

Acknowledgements

This work was supported by the National Natural Science Foundation of China (U21A20314, 22107089, 11974103, and 22378100); T. D. J. wishes to thank the University of Bath and the Open Research Fund of the School of Chemistry and Chemical Engineering, Henan Normal University (2020ZD01) for support. T. D. J. has been appointed as an Outstanding Talent by Henan Normal University. The work was supported by the Program for Innovative Research Team in Science and Technology at the University of Henan Province (23IRTSTHN002). J. Y. and W. J. J. thank the National Research Foundation of Korea for the grant funded by the Korean government (MSIT) (RS-2023-00217701). The Henan Province Central Leading Local Science and Technology Development Fund Project (Z20231811083) and the Central Government of Henan Province Guides Local Projects are acknowledged. All authors express their gratitude to Dr C. C. Shen for his invaluable assistance in this study.

Notes and references

1 L. Zhao, J. Li, Y. Su, L. Yang, L. Chen, L. Qiang, Y. Wang, H. Xiang, H. P. Tham, J. Peng and Y. Zhao, *Science Advances*, 2020, **6**, eaaz0575.
2 C. Lu, Z. Li, N. Wu, D. Lu, X.-B. Zhang and G. Song, *Chem*, 2023, **9**, 3185–3211.
3 T. C. Pham, V. N. Nguyen, Y. Choi, S. Lee and J. Yoon, *Chem. Rev.*, 2021, **121**, 13454–13619.
4 J. A. Figueira and V. C. Veltrini, *Photodiagn. Photodyn. Ther.*, 2017, **20**, 125–129.
5 C. Hopper, *Lancet Oncol.*, 2000, **1**, 212–219.
6 L. O. Svaasand and R. Ellingsen, *Photochem. Photobiol.*, 1983, **38**, 293–299.
7 D. Mao, W. Wu, S. Ji, C. Chen, F. Hu, D. Kong, D. Ding and B. Liu, *Chem*, 2017, **3**, 991–1007.
8 G. O. Schenck, *Ind. Eng. Chem.*, 1963, **55**, 40–43.
9 J. M. Brown, *Mol. Med. Today*, 2000, **6**, 157–162.
10 D. Hanahan and R. A. Weinberg, *Cell*, 2011, **144**, 646–674.
11 E. Hammond, M. C. Asselin, D. Forster, J. O'Connor, J. M. Senra and K. J. Williams, *Clin. Oncol.*, 2014, **26**, 277–288.
12 M. R. Detty, S. L. Gibson and S. J. Wagner, *J. Med. Chem.*, 2004, **47**, 3897–3915.
13 A. Juarranz, P. Jaén, F. Sanz-Rodríguez, J. Cuevas and S. González, *Clin. Transl. Oncol.*, 2008, **10**, 148–154.
14 E. H. C. van Dijk, T. J. van Rijssen, Y. Subhi and C. J. F. Boon, *Ophthalmol. Ther.*, 2020, **9**, 329–342.
15 Y. Liu, L. Scrivano, J. D. Peterson, M. Fens, I. B. Hernández, B. Mesquita, J. S. Toraño, W. E. Hennink, C. F. van Nostrum and S. Oliveira, *Mol. Pharm.*, 2020, **17**, 1276–1292.
16 K. Li, W. Dong, L. Qiu, Q. Liu, G. Lv, Y. Peng, M. Xie and J. Lin, *Eur. J. Med. Chem.*, 2019, **181**, 111582.
17 H. Gu, W. Liu, W. Sun, J. Du, J. Fan and X. Peng, *Chem. Sci.*, 2022, **13**, 9719–9726.
18 J. M. Beames, A. J. Hudson, T. D. Vaden and J. P. Simons, *Phys. Chem. Chem. Phys.*, 2010, **12**, 14076–14081.
19 J. Sun, K. Du, J. Diao, X. Cai, F. Feng and S. Wang, *Angew Chem. Int. Ed. Engl.*, 2020, **59**, 12122–12128.
20 M. Li, Y. Shao, J. H. Kim, Z. Pu, X. Zhao, H. Huang, T. Xiong, Y. Kang, G. Li, K. Shao, J. Fan, J. W. Foley, J. S. Kim and X. Peng, *J. Am. Chem. Soc.*, 2020, **142**, 5380–5388.
21 Q. Yao, J. Fan, S. Long, X. Zhao, H. Li, J. Du, K. Shao and X. Peng, *Chem*, 2021, **8**, 197–209.
22 Y. Y. Zhao, L. Zhang, Z. Chen, B. Y. Zheng, M. Ke, X. Li and J. D. Huang, *J. Am. Chem. Soc.*, 2021, **143**, 13980–13989.
23 L. Li, C. Shao, T. Liu, Z. Chao, H. Chen, F. Xiao, H. He, Z. Wei, Y. Zhu, H. Wang, X. Zhang, Y. Wen, B. Yang, F. He and L. Tian, *Adv. Mater.*, 2020, **32**, e2003471.
24 L. Zuo, W. Nie, S. Yu, W. Zhuang, G. Wu, H. Liu, L. Huang, D. Shi, X. Sui, Y. Li and H. Y. Xie, *Angew Chem. Int. Ed. Engl.*, 2021, **60**, 25365–25371.
25 V. N. Nguyen, Y. Yan, J. Zhao and J. Yoon, *Acc. Chem. Res.*, 2021, **54**, 207–220.

26 Y. Wang, S. Xu, L. Shi, C. Teh, G. Qi and B. Liu, *Angew Chem. Int. Ed. Engl.*, 2021, **60**, 14945–14953.
27 M. Wu, X. Liu, H. Chen, Y. Duan, J. Liu, Y. Pan and B. Liu, *Angew Chem. Int. Ed. Engl.*, 2021, **60**, 9093–9098.
28 P. Xiao, Z. Shen, D. Wang, Y. Pan, Y. Li, J. Gong, L. Wang, D. Wang and B. Z. Tang, *Adv. Sci.*, 2022, **9**, e2104079.
29 X. Zhao, J. Liu, J. Fan, H. Chao and X. Peng, *Chem. Soc. Rev.*, 2021, **50**, 4185–4219.
30 V. N. Nguyen, S. Qi, S. Kim, N. Kwon, G. Kim, Y. Yim, S. Park and J. Yoon, *J. Am. Chem. Soc.*, 2019, **141**, 16243–16248.
31 W. Zhou, S. Chen, Y. Ouyang, B. Huang, H. Zhang, W. Zhang and J. Tian, *Chem. Sci.*, 2023, **14**, 11481–11489.
32 A. Chevalier, Y. Zhang, O. M. Khdour, J. B. Kaye and S. M. Hecht, *J. Am. Chem. Soc.*, 2016, **138**, 12009–12012.
33 Y. Li, Y. Sun, J. Li, Q. Su, W. Yuan, Y. Dai, C. Han, Q. Wang, W. Feng and F. Li, *J. Am. Chem. Soc.*, 2015, **137**, 6407–6416.
34 A. Podder, V. P. Murali, S. Deepika, A. Dhamija, S. Biswas, K. K. Maiti and S. Bhuniya, *Anal. Chem.*, 2020, **92**, 12356–12362.
35 B. K. Kundu, G. Han and Y. Sun, *J. Am. Chem. Soc.*, 2023, **145**, 3535–3542.
36 N. Zhang, Y. Wang, S. Leng, S. Xu, L. Zhang, Q. Wang, Q. Zhang and H. Y. Hu, *Talanta*, 2019, **205**, 120133.
37 H. W. Liu, L. Chen, C. Xu, Z. Li, H. Zhang, X. B. Zhang and W. Tan, *Chem. Soc. Rev.*, 2018, **47**, 7140–7180.
38 X. Zhao, S. Long, M. Li, J. Cao, Y. Li, L. Guo, W. Sun, J. Du, J. Fan and X. Peng, *J. Am. Chem. Soc.*, 2020, **142**, 1510–1517.
39 A. Garten, S. Schuster, M. Penke, T. Gorski, T. de Giorgis and W. Kiess, *Nat. Rev. Endocrinol.*, 2015, **11**, 535–546.
40 H. Lv, G. Lv, C. Chen, Q. Zong, G. Jiang, D. Ye, X. Cui, Y. He, W. Xiang, Q. Han, L. Tang, W. Yang and H. Wang, *Cell Metab.*, 2021, **33**, 110–127.
41 T. Nacarelli, L. Lau, T. Fukumoto, J. Zundell, N. Fatkhutdinov, S. Wu, K. M. Aird, O. Iwasaki, A. V. Kossenkov, D. Schultz, K. I. Noma, J. A. Baur, Z. Schug, H. Y. Tang, D. W. Speicher, G. David and R. Zhang, *Nat. Cell Biol.*, 2019, **21**, 397–407.
42 X. Li, Y. L. Wang, C. Chen and Y. F. Han, *Chem.–Eur. J.*, 2023, **29**, e202203242.
43 Q. Wan, R. Zhang, Z. Zhuang, Y. Li, Y. Huang, Z. Wang, W. Zhang, J. Hou and B. Tang, *Adv. Funct. Mater.*, 2020, **30**, 2002057.
44 Y. A. Ilan, G. Czapski and D. Meisel, *Biochim. Biophys. Acta*, 1976, **430**, 209–224.
45 M. Berlanga, Brock Biology of Microorganisms, *Int. Microbiol.*, ed. M. T. Madigan and J. M. Martinko, 11th edn, Núm. 2, 2005, 2010, vol. 8, pp. 149–150.
46 S. Uchinomiya, R. Horobin, E. Alvarado-Martínez, E. Peña-Cabrera and Y.-T. Chang, *Comb. Chem. High Throughput Screening*, 2016, **19**, 378–383.
47 S. Pillai, I. Mahmud, R. Mahar, C. Griffith, M. Langsen, J. Nguyen, J. W. Wojtkowiak, P. Swietach, R. A. Gatenby, M. M. Bui, M. E. Merritt, P. McDonald, T. J. Garrett and R. J. Gillies, *Cell Rep.*, 2022, **39**, 110796.
48 A. R. Thiam and E. Ikonen, *Trends Cell Biol.*, 2021, **31**, 108–118.
49 T. Liang, D. Wen, G. Chen, A. Chan, Z. Chen, H. Li, Z. Wang, X. Han, L. Jiang, J. J. Zhu and Z. Gu, *Adv. Mater.*, 2021, **33**, e2100629.
50 B. R. Gastman, X. M. Yin, D. E. Johnson, E. Wieckowski, G. Q. Wang, S. C. Watkins and H. Rabinowich, *Cancer Res.*, 2000, **60**, 6811–6817.
51 J. A. Bertout, S. A. Patel and M. C. Simon, *Nat. Rev. Cancer*, 2008, **8**, 967–975.